Electronic and atomic structures of KFe$_2$Se$_2$ grain boundaries

Wei Fan *, Da-Yong Liu, Zhi Zeng

Key Laboratory of Materials Physics, Institute of Solid state Physics, Hefei Institutes of Physical Sciences, Chinese Academy of Sciences, 230031 Hefei, Anhui-Province, People's Republic of China

ARTICLE INFO

ABSTRACT

The electronic and atomic structures of the twist and tilt grain boundaries (GB) of the iron-based superconductor KFe$_2$Se$_2$ are studied based on the simulations of the first principles density functional theory. Our results have clarified that the $\Sigma5[001]$ twist grain boundary of KFe$_2$Se$_2$ with layered structure has the lower grain-boundary energy. The local structure and the main features of the basic electronic structure within the [001] twist grain-boundary region have small differences compared with those in KFe$_2$Se$_2$ crystal. The large fluctuations of the charges and magnetic moments are found in the [001] tilt grain-boundary regions, especially the former are more prominent. The bi-collinear anti-ferromagnetic order is the most stable magnetic order even with grain boundaries in the bulk. The $\sqrt{5}a \times \sqrt{5}a$ superstructure of Fe-vacancies in K$_2$Fe$_4$Se$_5$ phase is intrinsically related to the coincident-site lattice of $\Sigma5[001]$ twist grain boundary.

1. Introduction

Since the discovery of the LaFeAs (O,F) superconductor [1,2], the superconducting transition-temperature T_C of the iron-based superconductors has been improved the record higher than 55 K [3]. The high T_C of the iron-based superconductors provides new opportunities for the applications of superconductors in a wide range of fields. The role of grain boundary (GB) is an important issue for the applications of high-temperature superconductors [4,5]. Recently, the weak-link properties of grain boundaries have been studied in the films of the cobalt doped Ba-122 on the surfaces of bi-crystalline oxide insulators (MgO, STO, LSAT) [6–8]. There is a threshold value θ_C from 5° to 9° of grain-boundary angle θ_{GB}, where above θ_C the critical current decreases very rapidly with θ_{GB}. The almost constant critical current below $\theta_C = 9°$ indicates that the improvement of the epitaxial film of the iron-based superconductors is more flexible for the applications compared with cuprate high-temperature superconductors [6]. The θ_{GB} dependent critical current of cuprate superconductor has been theoretically studied by using tight-binding method [9], which concluded that the damages of square structures of CuO$_2$ layers near grain boundary were very essential to the reduction of critical current [9,10]. For the iron-based superconductors the iron ions form square lattices in Fe$_2$As$_2$ layers or Fe$_2$Se$_2$ layers so that the same explanation in Ref. [9] is still suitable to the critical-current reductions in the iron-based superconductors because both the iron-based superconductors and the cuprate superconductors generally have short

superconducting coherence lengths comparable with the widths of grain boundaries.

A great deal of theoretical work has been focused on the electronic structures of the crystal of the iron-based superconductors [11]. The information of the electronic structure of the iron-based superconductors is important to understand the superconducting mechanism and the interesting properties of normal state. On the other hand, the properties of the twin boundaries of Fe-pnictides superconductor are calculated based on two-orbital tight-binding model, and the enhanced (or suppressed) superconductivity is dependent on the arrangements of atoms at twin boundaries [12]. The first-principles density functional theory has rarely been used to investigate the grain-boundary properties of the iron-based superconductors so that at present it is urgent to do research along this direction.

The KFe$_2$Se$_2$ superconductor has many interesting properties such as the complex magnetic structures [13,14] and the phase separation of different crystal structures [15–18]. The $\sqrt{5}a \times \sqrt{5}a$ superstructures have been found in the observations of high resolution transmission electron microscopy (HRTEM) of K$_x$Fe$_{2-y}$Se$_2$ (K$_{0.8}$Fe$_{1.6}$Se$_2$ or K$_2$Fe$_4$Se$_5$) [16,19] which was explained as the superstructure of the iron vacancies with the blocked anti-ferromagnetic order [20,21].

In this work, we study the twist and tilt grain boundaries of the iron-based superconductor KFe$_2$Se$_2$ by using the first-principle density functional theory. We find that the [001] twist grain boundaries have lowest grain-boundary energy and have small influence on the basic electronic structure of KFe$_2$Se$_2$. Among the different magnetic orders included in the calculations of grain boundaries, the bi-collinear anti-ferromagnetic order (BIC AFM) is

* Corresponding author. Tel.: +86 0551 65591464; fax: +86 0551 65591434.
E-mail address: fan@theory.issp.ac.cn (W. Fan).

the most stable one in all grain-boundary models studied in this work. There are large magnetic and charge fluctuations near tilt ground-boundary regions which are disadvantaged to the transport of super-current. Just like the Morié pattern, the formation of the $\sqrt{5}a \times \sqrt{5}a$ superstructure found in HRTEM is intrinsically related to the coincident-site lattice of the twist $\Sigma 5[001]$ grain boundary.

2. Theoretical method and grain-boundary model

The electronic structures and atomic structures of the KFe_2Se_2 crystals and grain boundaries are calculated by using the first principles method based on density functional theory. The Kohn–Sham equation is solved by using the standard plane-wave pseudo-potential method [22], and especially the pseudo-potentials that describe the interactions between valence electrons and ion-cores are built by the Projected-Augment-Wave method [23,24]. The exchange–correlation functional adopts the generalized gradient approximation with the formulas of Perdew–Burke–Ernzerhof (PBE) functional [25]. The configurations of valence electrons are $3s^23p^64s^1$, $3d^64s^2$ and $4s^24p^4$ for K, Fe and Se respectively. The KFe_2Se_2 crystal that is built by K ions sandwiched between two Fe_2Se_2 layers has $I4/mmm$ (D_{4h}-17) space-group symmetry with lattice constants $a = b = 3.913$ Å, $c = 14.0367$ Å. The kinetic-energy cutoff of plane-wave is set to 268 eV. The only one Γ point is used for the integrations in the first Brillouin zone by considering the large simulation cell and the small first Brillouin zone.

In plane-wave pseudo-potential method, a periodic box is used to simulate an infinite atomic system. The coincident-site-lattice (CSL) model [26,27] is a good choice for the simulations of grain boundaries because the CSL model keeps the part of periodic structure of original crystal that makes it more easily to design simulation cells satisfying periodic boundary condition. The CSL grain boundaries are observed in a great of materials although not all grain boundaries could be assigned as CSL type. The grain-boundaries of the cuprate and iron-based high-temperature superconductors can be designed on the insulating oxide substrates with the desired type of CSL grain-boundary. The two crystals on both sides of grain-boundary plane have different orientations. In the CSL model, a grain boundary is formed by a rotation of two crystals with angle θ_{GB} around a rotation axis $[l, m, n]$. If initially the two crystals are completely coincided, after a rotation with a very specific rotation axis and a rotation angle, the parts of lattice sites of two crystals may be coincided. These coincident sites generally form a superstructure or super-lattice with a larger elementary cell with the volume that is an integer multiple Σ of that of original lattice. The Σ is an important parameter characterizing grain boundary and is determined by specific rotation axis and rotation angle. One Σ generally has more than one sets of rotation axis and rotation angle. The grain boundary is called tilt if the rotation axis is in grain-boundary plane and is named twist if rotation axis is perpendicular to grain-boundary plane. The two crystals on both sides of grain-boundary plane are permitted to have a displacement parallel to grain-boundary plane to optimize the structure of the grain boundary. For tetragonal structure ($a = b$), the [001] grain boundary is easily constructed with the same method as the crystal with cubic symmetry. Therefore we construct KFe_2Se_2 $\Sigma 5[001]$ tilt and twist grain-boundaries and $\Sigma 13[001]$, $\Sigma 17[001]$ and $\Sigma 29[001]$ tilt grain-boundaries with GB parameters summarized in Table 1. We can easily prove that $|3\vec{a} + 2\vec{b}| \cong |-2\vec{a} + 3\vec{b}| \cong |\vec{c}|$ so that we can artificially construct a $\Sigma 13[320]$ twist grain boundary with rotation axis $[320]$ and rotation angle $90°$. The structures of all grain boundaries in Table 1 are fully optimized with the volumes and shapes of simulation cells.

The grain-boundary energy is an important parameter to characterize the properties of grain boundary, which is defined as the formation energy per unit area, which is expressed as $E_{GB} = (1/2)(E - \sum_i n_i \mu_i)/A_{GB}$, where E is the total energy of whole grain-boundary, n_i is the number of i-type atom and μ_i the corresponding chemical potential in perfect KFe_2Se_2 crystal, A_{GB} is the area of grain-boundary plane and the factor $1/2$ is due to two grain-boundaries in the simulation cells. It is very difficult to obtain the exact chemical potential μ_i. In Ref. [28], the possible bounds of μ_i are defined for all types of atoms in materials. In this work, we try a different method to calculate μ_i, that is to take a value in a perfect KFe_2Se_2 lattice without grain boundary. The total energy of a perfect crystal can be artificially partitioned as the summation of the contributions of all atoms and written as $E_0 = \sum_p n_p \mu_p$, where E_0 is the total energy of the perfect crystal. The total energy will change μ_p if we remove a p-type atom. In the calculation of density functional theory, we can remove an atom from a perfect crystal and calculate the energy difference $\tilde{\mu}_p = E_0 - E_p$, where E_p is the total energy with a vacancy by removing a p-type atom. However, in real calculation we find $\widetilde{E}_0 = \sum_p n_p \tilde{\mu}_p \neq E_0$ because the self-interaction with the images of p vacancy due to periodic condition. It is demanded that $\tilde{\mu}_p \to \mu_p$ and $\widetilde{E}_0 \to E_0$ could be approved if the simulation cell increases

Table 1
The parameters of the tilt and twist grain boundaries studied in this work. The total energies E_T of grain-boundary models and the corresponding grain-boundary energies E_{GB} are calculated for five types of magnetic orders. Some of magnetic orders fail to cooperate with grain-boundary models are labeled with star '*' means that there are magnetic defects such as the examples in Fig. 6(f, h). The results of two perfect crystals C1 and C2 with different number of atoms are also present in the table.

	$\Sigma 5$	$\Sigma 5$	$\Sigma 5$	$\Sigma 13$	$\Sigma 13$	$\Sigma 17$	$\Sigma 29$	C1	C2
Type	Twist	Twist	Tilt	Twist	Tilt	Tilt	Tilt		
Axis	[001]	[001]	[001]	[320]	[001]	[001]	[001]		
Plane	(001)	(001)	($\bar{1}20$)	($3\bar{2}0$)	($\bar{1}50$)	($\bar{3}50$)	($\bar{2}50$)		
Angle	36.87°	36.87°	53.13°	90.00°	22.62°	61.93°	43.60°		
Natom	200	400	580	520	500	660	560	40	500
E_T (eV)									
Néel	−1079.85		−3129.99		−2698.14	−3558.13	−3015.84	−216.739	−2712.63
BIC			−3152.67	−2823.88	−2712.06*	−3575.75*	−3031.48*	−218.345	
Stripe	−1085.88	−2178.33	−3145.19		−2705.85	−3579.08	−3034.64*	−217.958	
FM	−1082.31		−3136.47		−2702.58	−3567.73	−3023.12	−217.447	−2722.73
NM	−1074.91		−3117.57		−2686.58	−3541.30	−3000.10		−2701.27
E_{GB} (J/m^2)									
Néel	0.279		0.564		0.429	0.588	0.628		
BIC			0.530	0.795	0.565*	0.767*	0.771*		
Stripe	0.302	0.399	0.666		0.661	0.595	0.601*		
FM	0.378		0.709		0.570	0.658	0.710		
NM	0.305		0.550		0.448	0.654	0.737		

infinitely. In current stage, we simply define $\mu_p = (E_0/\widetilde{E}_0)\tilde{\mu}_p$ by simple scaling $\tilde{\mu}_p$ so that the relation $E_0 = \sum_p n_p \mu_p$ is satisfied. Additionally it is more reliable that the size and the number of atoms in chosen perfect lattice are close to those of the grain-boundary model. As a very special case, for the [0 0 1] twist grain boundary, a perfect lattice with the same size, shape and the equal number of atoms for each element can be constructed so that the formula of grain-boundary energy is simply reduced to $(1/2)(E - E_0)/A_{GB}$ which is equivalent to the deformation energy of prefect lattice without loss of atoms. The grain-boundary energies adopted above approximations are summarized in Table 1.

3. The electronic and atomic structures of KFe₂Se₂ 5[0 0 1] twist grain boundaries

Experimentally, the [0 0 1] twist grain boundaries of cuprate superconductors have very small influence on the superconducting properties independent on the rotation angle [29] because the [0 0 1] twist boundaries may have small damages on the local atomic structures and electronic structures of cuprate superconductors. In this section, we investigate the atomic and electronic structures of the [0 0 1] twist grain boundaries of the iron-based superconductor KFe₂Se₂. Fig. 1 shows the cross section of the Σ5[0 0 1] twist grain-boundary that is formed by rotating two lattices about 36.87°. It is very important that the grain-boundary plane is parallel to the Fe₂Se₂ layer. The size of the elementary cell of CSL lattice is $\sqrt{5}a \times \sqrt{5}a$ within grain-boundary plane and the size of super-cell of our simulation model is $\sqrt{10}a \times \sqrt{10}a$ shown in Fig. 1. Two Σ5[0 0 1] twist grain-boundary models with sizes $\sqrt{10}a \times \sqrt{10}a \times 2c$ and $\sqrt{10}a \times \sqrt{10}a \times 4c$ are investigated in this work. The optimized structure of the model $\sqrt{10}a \times \sqrt{10}a \times 4c$ is plotted in Fig. 2(a).

Determination of the magnetic order plays an important role in understanding the properties of the iron-based superconductors. In this work, we consider five types of magnetic orders: (1) the Néel AFM (or checkerboard AFM), (2) the stripe AFM (or collinear AFM), (3) the bi-collinear (BIC) AFM, (4) the ferromagnetic order and (5) the non-magnetic order. In the calculations of the total energies of the KFe₂Se₂ crystals, the order of the stability is the bi-collinear AFM, the stripe AFM, the ferromagnetic order, the Néel AFM and non-magnetic order (Table 1). The ferromagnetic order is more stable than Néel AFM means that not all types of AFM orders are more stable than ferromagnetic order and the ferromagnetic order probably plays an important role in determining the magnetic structure of KFe₂Se₂. In fact the bi-collinear AFM has short-range ferromagnetic order, which in the most stable state with the lowest total

energy. However, the bi-collinear AFM can not be organized very well in our two Σ5[0 0 1] models due to the restrictions of the periodic boundary condition and the small simulation sizes within grain-boundary plane. From Table 1, the twist grain boundary with the stripe AFM order is more stable than others except for the bi-collinear AFM. The order of stability in Σ5[0 0 1] twist grain boundary model is the same as that in crystal.

There are two grain-boundaries in a twist grain-boundary model (one at the center and the other at boundaries) due to the periodic boundary condition along [0 0 1] direction. Generally the two grain boundaries have interactions that decease with increasing the distance between two grain boundaries. Compared the results (the stripe AFM) of $\sqrt{10}a \times \sqrt{10}a \times 2c$ model with those of $\sqrt{10}a \times \sqrt{10}a \times 4c$ model, we can see that the grain-boundary energies increase with increasing the distance between two grain boundaries. This means that two grain boundaries are attracted each other so that the interaction energy between grain boundaries is negative. Fig. 3(a–c) show the projected partial density of states of atoms within the region of grain boundary and that for the corresponding atoms in crystal. We can see that the density of states of Σ5[0 0 1] twist grain boundary has very small changes compared with those in crystal. This is consistent with the almost perfect interface structure of the Σ5[0 0 1] twist grain boundary shown in Fig. 2(a). The small influence on the basic electronic structure indicates that the Σ5[0 0 1] twist grain boundaries have small influence on the superconducting properties of the iron-based KFe₂Se₂ superconductor just like the role of [0 0 1] twist grain boundary in cuprate superconductors [29]. The perfect properties of twist [0 0 1] grain boundaries are closely relative to the fact that grain-boundary plane is parallel to Fe₂Se₂ layer and K layers so that the rotations of crystals have not damaged crystal structures.

4. The electronic structure of KFe₂Se₂/K₂Fe₄Se₅ twist interface

The super-lattices with modulation vectors $q = (3/5, 1/5, 0)$ and $(3/4, 1/4, 0)$ are found in the observation of the high resolution transmission electron microscopy (HRTEM) [19,16] and X-ray diffraction [30]. This means that the smallest elementary cell of the super-lattice has the based vectors [1 3 0] and [3 $\bar{1}$ 0] with size $\sqrt{10}a \times \sqrt{10}a$ (Fig. 1). The super-lattice is the sub-lattice of $\sqrt{5}a \times \sqrt{5}a$ coincident-site-lattice (CSL) as shown in Fig. 1. A neutron diffraction experiment [20] has proved that the novel magnetic order of $K_xFe_{2-y}Se_2$ is determined by a $\sqrt{5}a \times \sqrt{5}a$ super-structure of Fe-vacancies (FV), which is obviously the same as the ($\sqrt{5}a \times \sqrt{5}a$) Σ5 coincident-site lattice. The detail studies of the microstructure of $K_xFe_{2-y}Se_2$ show that the dominant phase is K₂Fe₄Se₅ and the superconducting phase is a three-dimensional network with filaments [17,18].

If $\sqrt{5}a \times \sqrt{5}a$ Fe-vacancy order exists in $K_xFe_{2-y}Se_2$ sample, what is the driving force to create this type of ordered structure? Near twist gain boundary, generally the lattice strain is large, therefore K, Fe and Se vacancies are more easily created near twist grain boundary by missing corresponding atoms. The distribution of strain near Σ5[0 0 1] twit grain boundary has the intrinsic $\sqrt{5}a \times \sqrt{5}a$ periodic modulations, so that the distributions of vacancies are easily created near this type of grain boundary and probably have the same type of modulation. We assume that a new type of Σ5[0 0 1] twist interface is created by above mechanism. The model in Fig. 4 is built by replacing the right grain of twist grain boundary in Fig. 2(a) by a grain of K₂Fe₄Se₅ with $\sqrt{5}a \times \sqrt{5}a$ Fe-vacancy order. The left grain without Fe-vacancies (NFV) has stripe AFM and the right grain with Fe-vacancies (FV) has the blocking AFM [20]. This construction is reasonable because some experiments have shown that the NFV and FV phases can be stacked along c-axis [16] to form super-lattice. We obtain the stable structure by
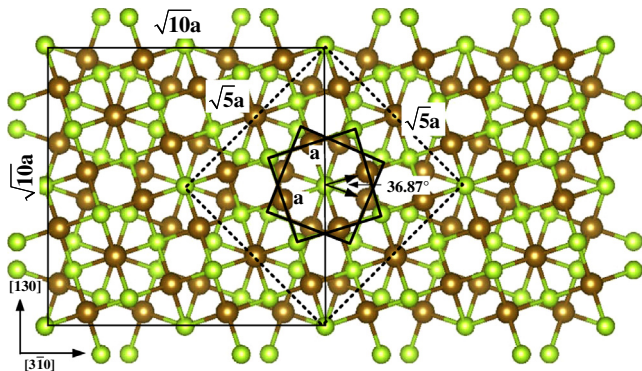

Fig. 1. The schematic diagram of twist Σ5[0 0 1] grain boundary. Two small thick squares (the elementary cells of original lattice) illustrate the rotation of two original lattices. The large dash-line $\sqrt{5}a \times \sqrt{5}a$ square is the elementary cell of CSL lattice that has the volume of five times of the elementary cell of original lattice. The $\sqrt{10}a \times \sqrt{10}a$ square is the real shape and size of the simulation cell.
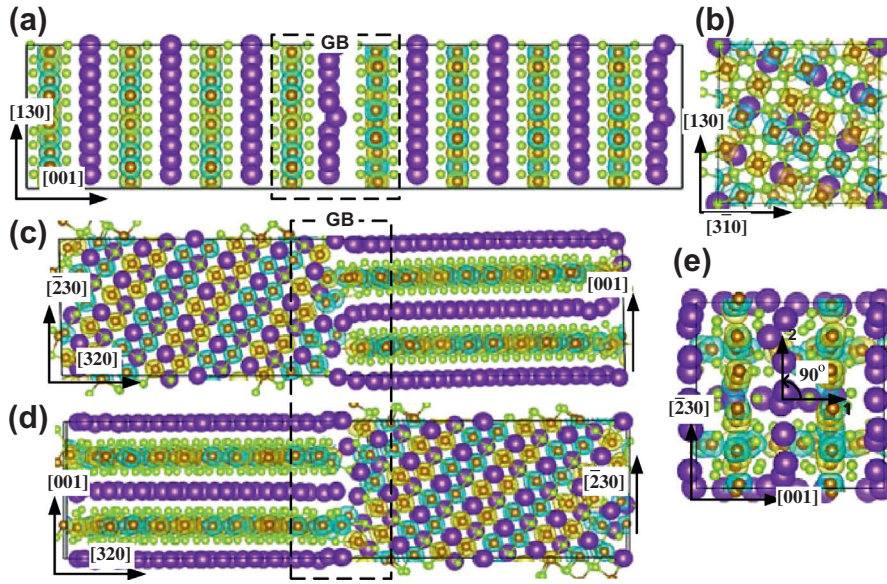
Fig. 2. The side view (a) and the top view (b) along [001] c-axis of the twist Σ5[001] grain boundary. The side views (c and d) and top view (e) of the twist Σ13[320] grain boundary along [320] direction. The magnetic densities are plotted together with structures. The iso-value of magnetic density is ±0.005 μ_B/Å³. The negative and positive magnetic densities are plotted with different colors: blue and dark-yellow respectively. The two dash-boxes show the grain-boundary regions of two grain-boundary models. (For interpretation of the references to colour in this figure legend, the reader is referred to the web version of this article.)
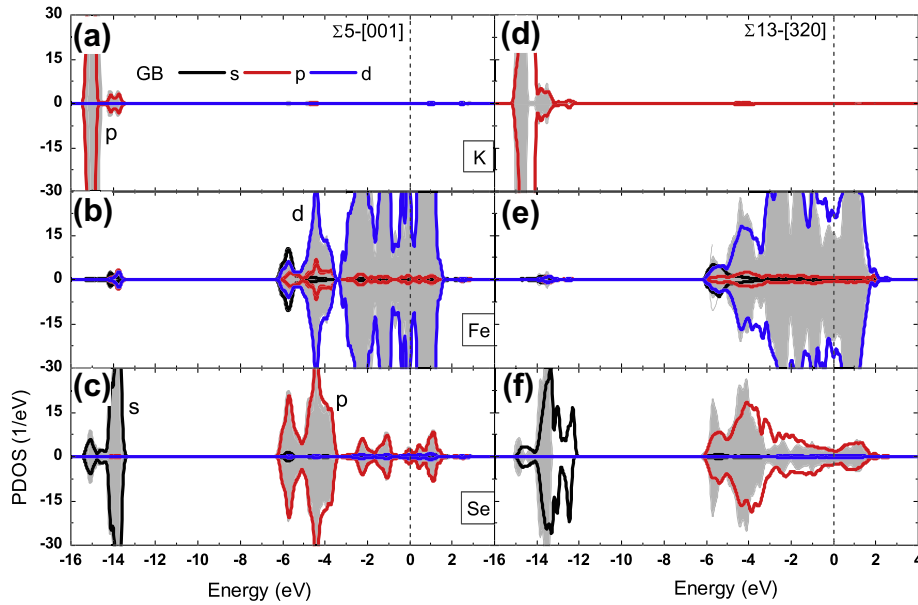

Fig. 3. The projected partial densities of states within the grain-boundary regions of the twist Σ5[001] and the twist Σ13[320] grain boundaries are plotted together with the corresponding density of states in perfect crystal as comparisons. The Fermi energies are set to zero and illustrated by vertical dash-lines, the dark filled curves are the density of states in perfect crystal.

fully structural optimization, which is stable even with large perturbations. We find that the K-layer in the center is not flat after structural optimization. Near the right grain boundary, K-layer losing two K atoms is flat in Fig. 4(e). This means that the interface strain will be released by missing some of atoms in the interface region. The stripe AFM order in left grain Fig. 4(e) and blocking AFM order in right grain Fig. 4(d) are still stable just like in crystal.

Experimentally, the FV phase is semiconductor with the electric resistivity about 10^5 Ω cm at 50 K which is eight orders of magnitude of the normal-state electric resistivity of the superconducting phase [31]. The semiconducting character of FV phase is additionally proved by the calculations of density functional theory [32]. The densities of states of the FV phases near twist interface in

Fig. 5(b) show that the behavior of FV phase is still semiconductor just like in crystal with energy gap about 0.5 eV. Besides the energy gap of the FV phase as a semiconductor, the NFV phase has an energy gap from −4.0 eV to −3.0 eV below Fermi energy in Fig. 5(a). The d orbitals of Fe atoms and p orbitals of Se atoms are almost equally occupied below the gap. This means that the electrons below the gap form covalent bond between Fe atom and Se atom. Above the gap, most electrons occupy d orbitals of Fe and the number of p electrons of Se atoms is small. Fig. 5(b) shows that the formation of Fe-vacancy makes the gap disappear and the density of states of p electrons of Se atoms at energy above the gap increases significantly. The density of states of the FV phase is very similar to that of oxide semiconductor such as ZnO.
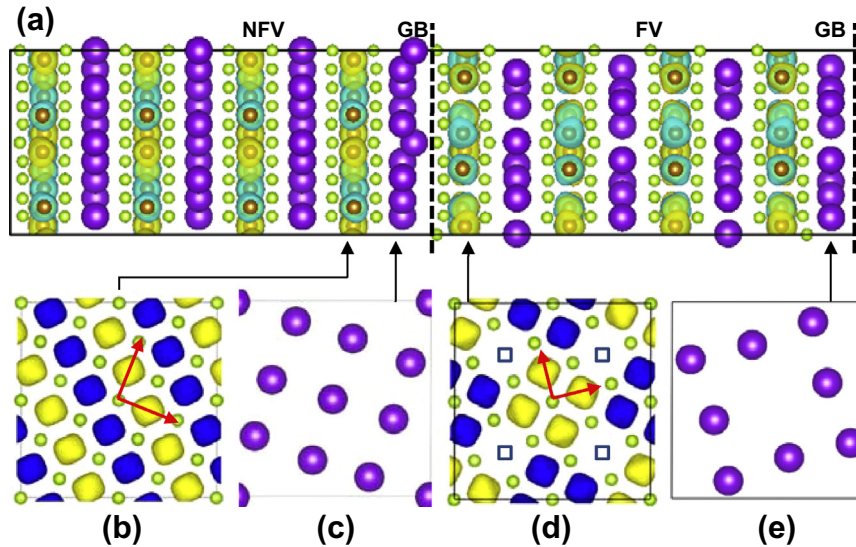
Fig. 4. (a) The twist $\Sigma5[001]$ grain boundary with $\sqrt{5}a \times \sqrt{5}a$ ordered Fe-vacancies in the right grain. Two thick dash-lines are the positions of two grain boundaries. The magnetic densities near grain-boundary plane are plotted, (b) in left Fe_2Se_2 layer, (d) right $FeSe_2$ layer, (c and e) in two K layers as illustrated by four arrows. The four small squares in (d) are Fe vacancies. The yellow and blue iso-surfaces are the spin-up and spin-down magnetic densities with iso-values ±0.01 $\mu_B/\text{Å}^3$. (For interpretation of the references to colour in this figure legend, the reader is referred to the web version of this article.)
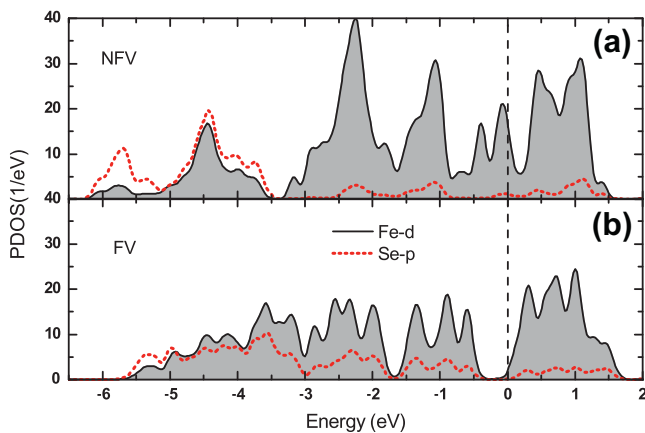
Fig. 5. The projected partial densities of states of the left Fe_2Se_2 layer in Fig. 4(b) without Fe-vacancies (NFV), and the right $FeSe_2$ layer in Fig. 4(d) with Fe-vacancies (FV). The black filled-curves are the PDOS of d-electrons of Fe atoms, and the red dot-curves are the PDOS of the p-electrons of Se atoms. The dash-line is Fermi energy.

5. The electronic and atomic structures of KFe_2Se_2 13[320] twist grain boundary

The lattice constants of iron-based KFe_2Se_2 superconductor have an approximate relation $|3\vec{a} + 2\vec{b}| = |-2\vec{a} + 3\vec{b}| \cong |\vec{c}|$, so that we can artificially construct a $\Sigma13[320]$ twist grain boundary with the rotation angle $90°$. The size of the simulation model is $\sqrt{13}a \times c \times 4\sqrt{13}a$. Fig. 2(c–e) show the optimized structure of the $\Sigma13[320]$ twist grain boundary. The bi-collinear AFM can be organized well in the model. From Fig. 3(d–f), the projected partial density of states within the region of grain boundary is very different from those in crystal with the same magnetic order. Very different from the $\Sigma5[001]$ twist grain boundaries, $\Sigma13[320]$ twist grain boundary changes the basic electronic structure of KFe_2Se_2 superconductor and will influence the superconducting properties of KFe_2Se_2. The significant modifications of electronic structures neighboring grain boundary are the direct reflection of the large modifications of lattice structure neighboring grain boundary

shown in Fig. 2(c and d). Additionally, the grain-boundary energy of the $\Sigma13[320]$ twist grain boundary is higher than those of all $\Sigma5[001]$ twist grain boundaries in Table 1. It is interesting that, if the super-current flows in Fe_2Se_2 layer, the super-current across the grain boundary will be very small because the Fe_2Se_2 layer at one side of the grain-boundary plane is perpendicular to the Fe_2Se_2 layer at the other side. As contrast, a very specific $\Sigma3[010]$ twist grain boundary of YBCO with rotation angle $90°$ has small influence on super-current flowing across the grain-boundary plane [33,34]. The perfect properties of the $\Sigma3[010]$ twist grain boundary is determined by the perovskite-type structure of YBCO superconductor and specific geometric relations of lattice constants $3a \cong 3b \cong c$.

6. The electronic and atomic structures of KFe_2Se_2 [001] tilt grain boundary

Experimentally, the critical current remains constant with grain-boundary angle θ_{GB} up to $9°$ for cobalt-doped $BaFe_2As_2$ epitaxial films fabricated on MgO [001] tilt bi-crystal substrate [6]. For the low-angle grain boundaries with $\theta_{GB} < 15°$, the distances between grain-boundary dislocations are large and the interactions between them are weak. With increasing θ_{GB}, the distances between dislocations are small and the interactions between dislocations are strong. In this section we study the electronic and atomic structures of high-angle grain boundaries with $\theta_{GB} > 20°$. The high-angle grain boundaries generally are weak links for cuprate superconductors and iron-based superconductors [7]. Our studies focus on the four types of tilt CSL high-angle grain boundaries $\Sigma5[001]$, $\Sigma13[001]$, $\Sigma17[001]$ and $\Sigma29[001]$ with grain-boundary parameters summarized in Table 1. The optimized structures and corresponding magnetic densities are plotted in Fig. 6(a–h). The five types of magnetic orders including (1) the Néel (or checkerboard) AFM, (2) bi-collinear (BIC) AFM, (3) the stripe (or collinear) AFM, (4) the ferromagnetic order and (5) non-magnetic order are considered in our calculations. Due to the small sizes of simulation cells and periodic boundary condition, some of magnetic orders are not perfect such as the magnetic configurations in Fig. 6(f, h). The bi-collinear AFM order is not cooperative very well with the $\Sigma13[001]$, $\Sigma17[001]$ and $\Sigma29[001]$ models. The perfect bi-collinear AFM has
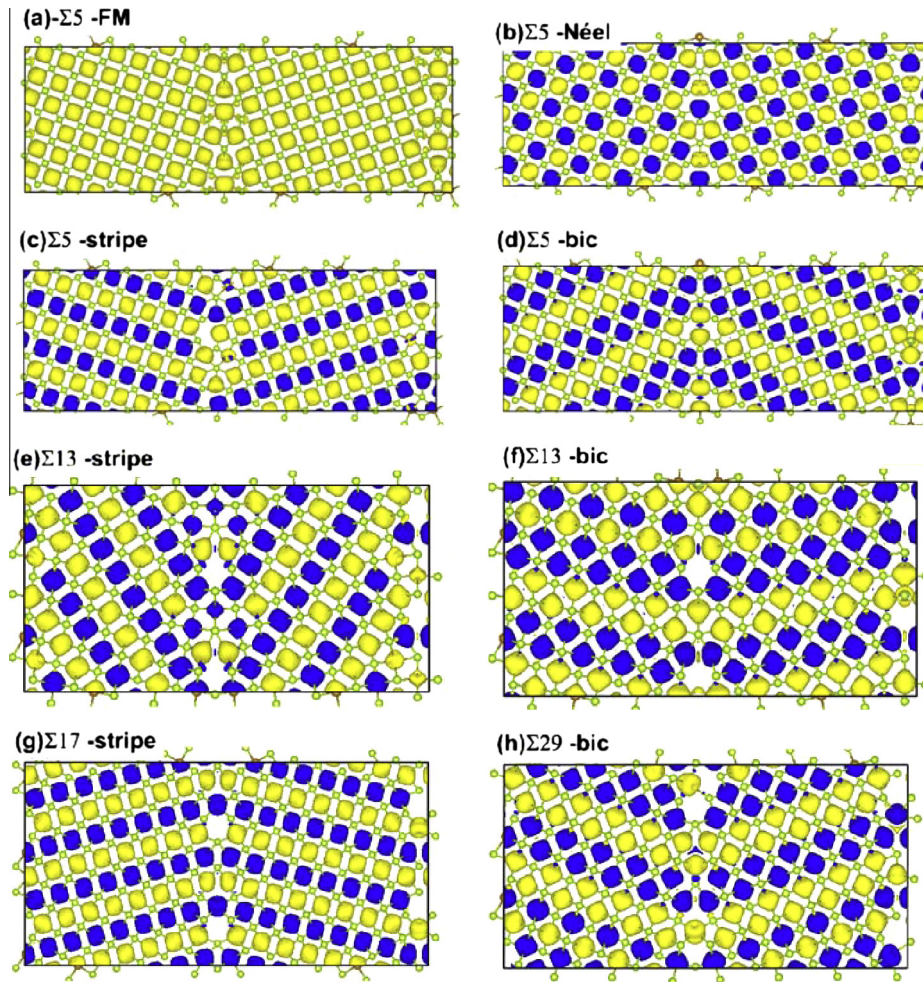
Fig. 6. The optimized structures and magnetic density of four [001] tilt grain boundaries ($\Sigma5, \Sigma13, \Sigma17, \Sigma29$) with different magnetic orders. The iso-value of magnetic density is ±0.005 $\mu_B/\text{Å}^3$. The negative and positive magnetic densities are plotted with different colors: blue and yellow respectively. (For interpretation of the references to colour in this figure legend, the reader is referred to the web version of this article.)

the continuous stacking of the two rows of spin-up Fe atoms and two rows of spin-down Fe atoms. We introduce the stacking faults in Fig. 6(f, h) with two single-rows of spin-up Fe atoms and spin-down Fe atoms to cooperative with periodic condition. From Fig. 6(a–h) we can see that magnetic orders are very robust with the existence of grain boundaries. Just like in crystal the bi-collinear AFM is the most stable magnetic order in all our grain-boundary models. This indicates that the bi-collinear AFM is stable even in polycrystalline. All the five types of magnetic orders are cooperative very well with the tilt $\Sigma5[001]$ grain boundary. For different magnetic orders, the optimized structures are different as shown in Fig. 6(a–d). The structure with stripe AFM is asymmetric after the structural relaxation. This means the magnetic interaction has significant influence on grain-boundary structure of iron-based KFe_2Se_2 superconductor. The grain-boundary energies of [001] tilt grain boundaries between 0.4 and 0.8 (J/m^2) are higher than those of [001] twist grain boundaries between 0.2 and 0.4 (J/m^2) in our calculations. This means that the [001] tilt grain boundaries are more difficult to form than the corresponding twist grain boundaries in KFe_2Se_2 film.

We calculate the effective charges of all atoms in our grain-boundary models, which is defined as $Z_e = Z_b - Z_0$, where Z_b is the number of valence electron obtained from Bader analysis [35] and Z_0 the number of valence electron of isolated atom. The magnetic moments M_b are calculated as the difference of the number

of spin-up and spin-down electrons in the partition regions obtained by the Bader analysis of charge densities. Fig. 7(a) and Fig. 7(b) show the distributions of effective charges and magnetic moments respectively across the tilt $\Sigma5[001]$ grain boundary with all five types of magnetic orders. The large charge and magnetic fluctuations are found near the grain-boundary regions. This is because the type and number of the nearest neighbor atoms and the bond lengths between atoms in grain-boundaries are different from those in the bulk so that the charge distribution, the exchange interaction and the orbital occupation are different. The bi-collinear AFM order and ferromagnetic order have the largest magnetic moments. The differences of magnetic moments steadily decrease until very close to grain-boundary plane. The fluctuations of charges are more significant than those of magnetic moments. Fig. 8(a–l) show the projected partial density of states within grain-boundary region and that in the bulk as a comparison. The sharp peaks of density of states in the bulk become dump and flat within grain-boundary region. For different magnetic orders, the density of states is different both in grain boundary and in the bulk. There exist the energy gaps of the d-electron of Fe atoms and the p-electron of Se atoms from −4.0 eV to −3.0 eV below Fermi energy for the stripe and Néel AFM orders, which is blurred in the grain-boundary regions. The gap has been discussed in Section 4. The electronic states of bi-collinear AFM are more dispersive and more metal-like compared with other anti-ferromagnetic orders. Fig. 9(a) and Fig. 9(b)
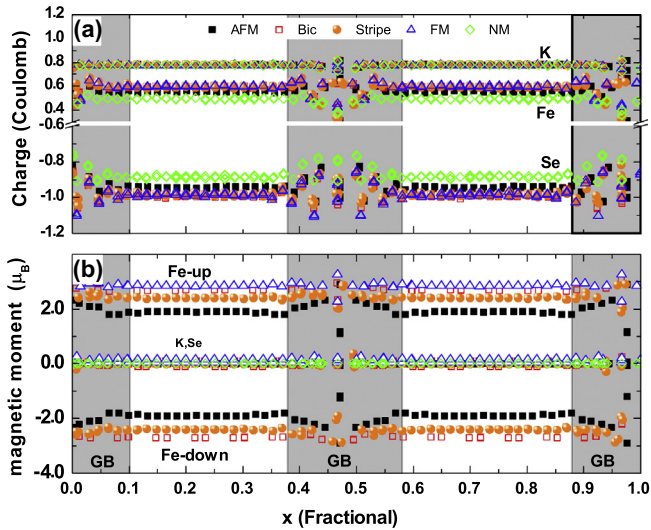
Fig. 7. The profiles of effective charges (a) and magnetic moments (b) across to the Σ5[001] tilt grain-boundary plane for the five types of magnetic orders in Fig. 6(a–d). The dark filled regions illustrate the grain-boundary regions.

show the distributions of effective charges and magnetic moments for all four grain-boundary models with Néel AFM (or checkerboard) order. The Néel AFM order is cooperative very well with all four grain-boundary models without magnetic defects. The fluctuations of charges are more significant than fluctuations of magnetic moments for all four grain-boundaries. The energy gaps near within [−4, −3] (eV) are blurred for all four grain-boundaries shown in Fig. 10. Based on the calculations in this section, the high-angle grain boundaries studied in this work have very similar properties. No simple rule is found for the θ_{GB}-dependent properties of KFe$_2$Se$_2$ superconductor with high-angle grain boundaries.

7. Summary

The twist [001] grain boundary of superconductor with layered structure has small grain-boundary energy and small influence on

the local crystal structure of superconductors. The basic electronic structure of superconducting material keeps almost unchanged by introducing the twist [001] grain-boundaries. The good properties of the [001] twist grain boundary are lost for the twist grain boundaries with rotation axis perpendicular to [001] c-axis, such as Σ13[320], because the rotations generally damage the Fe$_2$Se$_2$ layers. By the structural analysis of the Σ5[001] twist grain-boundary in detail, we find the intrinsic relation between the coincident-site-lattice of Σ5 twist grain boundary and the super-lattices found in HRTEM images of K$_x$Fe$_{2-y}$Se$_2$. The strain near grain boundary will drive the formation of lattice defect by releasing some atoms near grain-boundary plane. The K atoms near grain-boundary plane in Fig. 2(a) are easily lost with x < 1.0 to form K vacancies and modify the lattice structure of K layer in Fig. 4(e). However, the correspondence between two type of super-structures is not completely understood.

The [001] tilt high-angle grain boundaries have larger but very limited influence on the basic electronic structure than those of the twist [001] grain boundary. Just as the cuprate superconductors, to understand the role of weak-link of high-angle grain boundary of KFe$_2$Se$_2$ and other iron-based superconductors, we must understand their superconducting state. The superconducting coherence length about several nm is comparable or shorter than the grain-boundary width so that the existences of grain-boundaries will influence the superconducting properties significantly. The square structures of Fe$_2$Se$_2$ layer similar to the square structure in CuO$_2$ layer in YBCO are destroyed in the region of tilt grain boundary. The super-current density is significantly decreased because the square structures are correlated to the formation of coherent Cooper-pairs.

We study the grain-boundary structures by considering different magnetic structures. Similar to that in the bulk, the bi-collinear AFM order has the lowest total energy for all grain-boundary models considered in this work. The non-magnetic orders generally have the highest total energies. It is interesting that total energy of ferro-magnetic order is lower than that of Néel AFM and close to that of stripe AFM. The short range ferro-magnetic order may exist in KFe$_2$Se$_2$ such as the short-range ferromagnetic order in the bi-collinear AFM and the ferro-magnetic block for the novel block anti-ferromagnetic state in K$_2$Fe$_4$Se$_5$ [20].
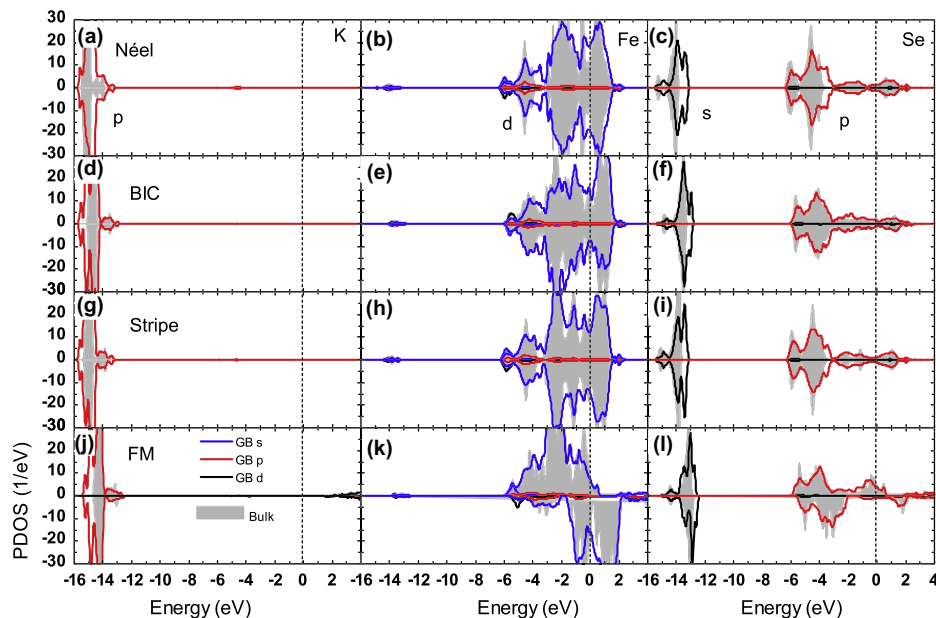
Fig. 8. The projected partial density of states of Σ5[001] tilt grain boundaries in Fig. 6(a–d) with different magnetic orders: (a–c) Néel order, (d–f) BIC order, (g–i) Strip order, (j–l) FM order. The dark filled curves are the corresponding density of states in perfect crystal. The vertical dash-lines illustrate the Fermi energy set to zero.
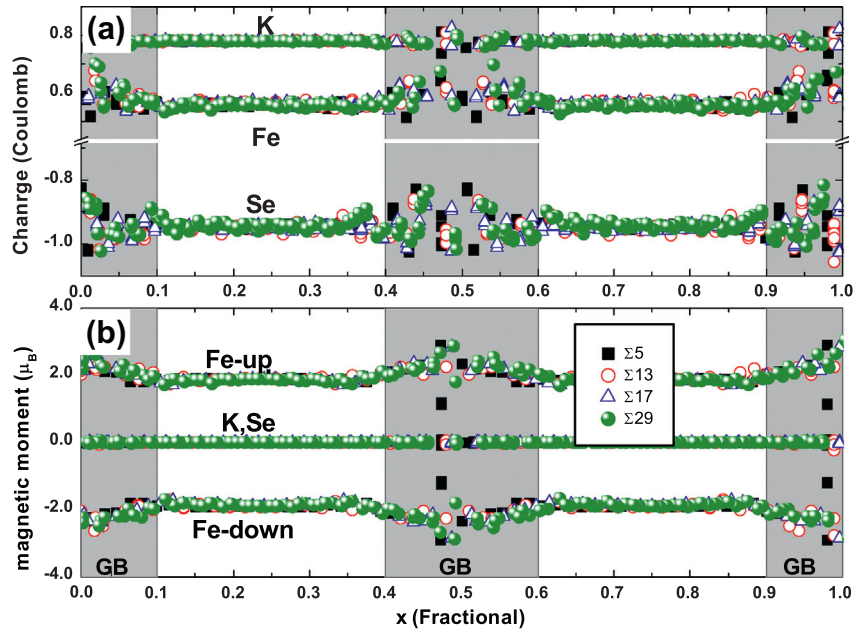
Fig. 9. The profiles of effective charges (a) and magnetic moments (b) across to four types of the [0 0 1] tilt grain-boundaries ($\Sigma 5, \Sigma 13, \Sigma 17, \Sigma 29$) with Néel type anti-ferromagnetic order. The dark filled regions illustrate the grain-boundary regions.
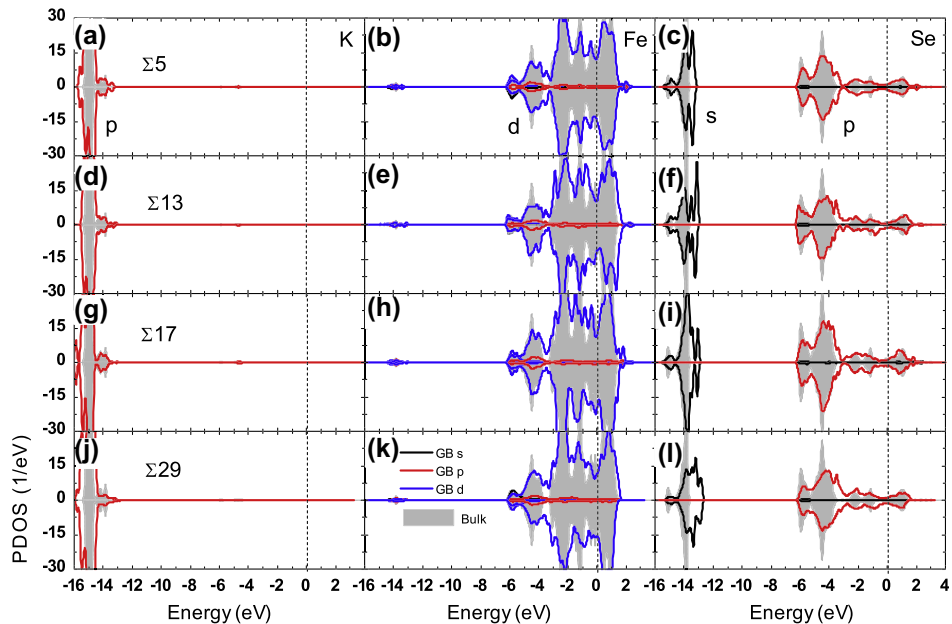
Fig. 10. The projected partial density of states of the four types of the [0 0 1] tilt grain boundaries ($\Sigma 5, \Sigma 13, \Sigma 17, \Sigma 29$) with Néel anti-ferromagnetic order: (a–c) $\Sigma 5$, (d–f) $\Sigma 13$, (g–i) $\Sigma 17$, (j–l) $\Sigma 29$. The dark-filled curves are the corresponding density of states in perfect crystal. The vertical dash-lines illustrate the Fermi energy set to zero.

Acknowledgements

References

[1] Y. Kamihara, T. Watanabe, M. Hirano, H. Hirano, J. Am. Chem. Soc. 130 (2008) 3296.
[2] X.H. Chen, T. Wu, G. Wu, R.H. Liu, H. Chen, D.F. Fang, Nature 453 (2008) 761.
[3] Z.-A. Ren et al., Chin. Phys. Lett. 25 (2008) 2215.
[4] H. Hilgenkamp, J. Mannhart, Rev. Mod. Phys. 74 (2002) 485.
[5] J.H. Durrell, C.-B. Eom, A. Gurevich, E.E. Hellstrom, C. Tarantini, A. Yamamoto, D.C. Larbalestier, Rep. Prog. Phys. 74 (2011) 124511.
[6] T. Katase, Y. Ishimaru, A. Tsukamoto, H. Hiramatsu, T. Kamiya, K. Tanabe, H. Hosono, Nat. Commun. 2 (2011) 409.

[7] S. Lee, J. Jiang, J.D. Weiss, C.M. Folkman, C.W. Bark, C. Tarantini, A. Xu, D. Abraimov, A. Polyanskii, C.T. Nelson, Y. Zhang, S.H. Baek, H.W. Jang, A. Yamamoto, F. Kametani, X.Q. Pan, E.E. Hellstrom, A. Gurevich, C.B. Eom, D.C. Larbalestier, Appl. Phys. Lett. 95 (2009) 212505.

[8] S. Schmidt, S. Doring, F. Schmidl, V. Tympel, S. Haindl, K. Iida, F. Kurth, B. Holzapfel, P. Seidel, IEEE Trans. Appl. Supercond. 23 (2013) 7300104.

[9] S. Graser, P.J. Hirscheld, T. Kopp, R. Gutser, B.M. Anderson, J. Mannhart, Nat. Phys. 6 (2010) 609.

[10] W. Fan, Z. Zeng, Physica C 471 (2011) 1606.

[11] I.I. Mazin, D.J. Singh, M.D. Johannes, M.H. Du, Phys. Rev. Lett. 101 (2008) 057003.

[12] Bo Li, Jian Li, K.E. Bassler, C.S. Ting, New J. Physc. 15 (2013) 103018. arXiv:1211.2855 [cond.mat.supr-con] 2012.

[13] E. Dagotto, Rev. Mod. Phys. 85 (2013) 849. arXiv:1104.5340 [cond.mat.supr-con] 2011.

[14] X.W. Yan, M. Gao, Z.Y. Lu, T. Xiang, Phys. Rev. B 84 (2011) 054502.

[15] W. Li, H. Ding, Z. Li, P. Deng, K. Chang, K. He, S.H. Ji, L.L. Wang, X.C. Ma, J.P. Hu, X. Chen, Q.K. Xue, Phys. Rev. Lett. 109 (2012) 057003.

[16] Y.J. Yan, M. Zhang, A.F. Wang, J.J. Ying, Z.Y. Li, W. Qin, X.G. Luo, J.Q. Li, J.P. Hu, X.H. Chen, Sci. Rep. 2 (2012) 212.

[17] S.C. Speller, T.B. Britton, G.M. Hughes, A. Krzton-Maziopa, E. Pomjakushina, K. Conder, A.T. Boothroyd, C.R.M. Grovenor, Supercond. Sci. Technol. 25 (2012) 084023.

[18] X.X. Ding, D.L. Fang, Z.Y. Wang, H. Yang, J.Z. Liu, Q. Deng, G.B. Ma, C. Meng, Y.H. Hu, H.H. Wen, Nat. Commun. 4 (2013) 1897.

[19] Z. Wang, Y.J. Song, H.L. Shi, Z.W. Wang, Z. Chen, H.F. Tian, G.F. Chen, J.G. Guo, H.X. Yang, J.Q. Li, Phys. Rev. B 83 (2001) 140505 (R).

[20] W. Bao, Q.Z. Huang, G.F. Chen, M.A. Green, D.M. Wang, J.B. He, Y.M. Qiu, Chin. Phys. Lett. 28 (2011) 086104.

[21] F. Ye, S. Chi, W. Bao, X.F. Wang, J.J. Ying, X.H. Chen, H.D. Wang, C.H. Dong, Minghu Fang, Phys. Rev. Lett. 107 (2011) 137003.

[22] G. Kresse, J. Furthmüller, Phys. Rev. B 54 (1996) 11169.

[23] G. Kresse, D. Joubert, Phys. Rev. B 59 (1999) 1758.

[24] P.E. Blöchl, Phys. Rev. B 50 (1994) 17953.

[25] J.P. Perdew, K. Burke, M. Ernzerhof, Phys. Rev. Lett. 77 (1996) 3865.

[26] A.P. Sutton, R.W. Balluffi, Interface in Crystalline Materials, Clarendon Press, Oxford, 1995.

[27] R.W. Balluffi, Metall. Trans. B 13 (1982) 527.

[28] S.B. Zhang, J.E. Northrup, Phys. Rev. Lett. 67 (1991) 2339.

[29] Qiang Li, Y.N. Tsay, Y. Zhu, M. Suenaga, G.D. Gu, N. Koshizuka, Supercond. Sci. Technol. 12 (1999) 1046.

[30] P. Zavalij, W. Bao, X.F. Wang, J.J. Ying, X.H. Chen, D.M. Wang, J.B. He, X.Q. Wang, G.F. Chen, P.Y. Hsieh, Q. Huang, M.A. Green, Phys. Rev. B 83 (2011) 132509.

[31] J.Q. Li, Y.J. Song, H.X. Yang, Z. Wang, H.L. Shi, G.F. Chen, Z.W. Wang, Z. Chen, H.F. Tian, arXiv:1104.5340 [cond-mat.supr-con], 2011.

[32] X.W. Yan, M. Gao, Z.Y. Lu, T. Xiang, Phys. Rev. Lett. 106 (2011) 087005.

[33] S.E. Babcock, X.Y. Cai, D.L. Kaiser, D.C. Larbalestier, Nature 347 (1990) 167.

[34] C.B. Eom, A.F. Marshall, Y. Suzuki, B. Boyer, R.F.W. Pease, T.H. Geballe, Nature 353 (1991) 544.

[35] G. Henkelman, A. Arnaldsson, H. Jónsson, Comput. Mater. Sci. 36 (2006) 354–360.

[36] K. Momma, F. Izumi, J. Appl. Crystallogr. 41 (2008) 653.